

1 Inner Magnetospheric Response to the IMF B_y 2 Component: Van Allen Probes and Arase Observations

3 N. A. Case¹, D. P. Hartley², A. Grocott¹, Y. Miyoshi³, A. Matsuoka⁴, S.
4 Imajo³, S. Kurita⁵, I. Shinohara⁶, and M. Teramoto⁷

5 ¹Department of Physics, Lancaster University, Lancaster, UK

6 ²Department of Physics and Astronomy, University of Iowa, Iowa City, IA, USA

7 ³Institute for SpaceEarth Environmental Research, Nagoya University, Nagoya, Japan

8 ⁴Graduate School of Science, Kyoto University, Kyoto, Japan

9 ⁵Research Institute for Sustainable Humanosphere, Kyoto University, Kyoto, Japan

10 ⁶Institute of Space and Astronautical Science, JAXA, Japan

11 ⁷Kyushu Institute of Technology, Kitakyushu, Japan

12 Key Points:

- 13 • The influence of IMF B_y is observed throughout the inner magnetosphere, using
14 Van Allen Probes and Arase observations
- 15 • The median ratio of the change in observed B_y to IMF B_y is ~ 0.33 , though a
16 clock angle dependence is found
- 17 • We find a consistent effect across both hemispheres, all MLT sectors, and all ra-
18 dial distances

Corresponding author: N. A. Case, n.case@lancaster.ac.uk

Abstract

We utilise 17 years of combined Van Allen Probes and Arase data to statistically analyse the response of the inner magnetosphere to the orientation of the IMF B_y component. Past studies have demonstrated that the IMF B_y component introduces a similarly oriented B_y component into the magnetosphere. However, these studies have tended to focus on field lines in the magnetotail only reaching as close to Earth as geosynchronous orbit. By exploiting data from these inner magnetospheric spacecraft, we have been able to investigate the response at radial distances of $< 7R_E$. When subtracting the background magnetic field values, provided by the T01 and IGRF magnetic field models, we find that the IMF B_y component does affect the configuration of the magnetic field lines in the inner magnetosphere. This control is observed throughout the inner magnetosphere, across both hemispheres, all radial distances, and all MLT sectors. The ratio of IMF B_y to observed B_y residual, also known as the “penetration efficiency”, is found to be ~ 0.33 . The IMF B_z component is found to increase, or inhibit, this control depending upon its orientation.

1 Introduction

The presence of a non-zero y -component in the interplanetary magnetic field (IMF B_y) has been shown to modify the topology of the magnetic field in Earth’s magnetosphere. First observed by Fairfield (1979), a positive IMF B_y component increases the y -component of the background magnetospheric field whilst a negative IMF B_y component results in a net decrease.

It has been reported that this effect is not uniform throughout the magnetosphere. Instead, the exact amount by which a non-zero IMF B_y component contributes to the local magnetic field in the magnetosphere has been shown to vary by location, dipole tilt and the sign of IMF B_z . For example, Fairfield (1979) found an average “penetration efficiency” of the IMF B_y component of 0.13, using data from IMP-6 spacecraft recorded between $-20R_E$ and $-33R_E$ downtail. That is to say that the change in the local B_y component is 0.13 times the value of the IMF B_y component. Numerous subsequent studies, from different regions of the magnetosphere, have been undertaken showing a broadly similar result but with different penetration efficiencies. For example, Cowley and Hughes (1983) and Nagai (1987) both used data from geostationary satellites (ATS 6 and GOES 6) and found penetration efficiencies of 0.28 and 0.3, respectively. Wing et al. (1995), however, showed that the penetration efficiency at geosynchronous orbit was much higher, varying between 0.52 and 0.60 depending if the data were recorded in the dayside or nightside magnetosphere. A study by Kaymaz et al. (1994), using IMP-8 data, found the “average perturbation” of the local B_y field to be 0.26 times the concurrent IMF B_y strength in the $-25R_E < X_{GSM} < -40R_E$ and $|Z_{GSM}| < 8R_E$ region. Studies from the plasma sheet region of the magnetosphere have observed penetration efficiencies around 0.50-0.60 (e.g. Lui, 1984; Petrukovich, 2009).

Particularly with more historic studies, the determination of the background local B_y field value was problematic. In most cases, it was simply determined using an average of the spacecraft data recorded during geomagnetically “quiet” conditions (i.e. when both the solar wind speed and IMF strength were low). More recent works utilise sophisticated magnetic field models to determine the background field, for example Tsyganenko and Andreeva (2020) implement the radial basis function model of Andreeva and Tsyganenko (2016) to determine the background field. In that work, data from an array of spacecraft missions were compared to determine the effect of IMF B_y at radial distances, $r > 5R_E$. The penetration efficiency was found to depend both on location and on the strength and orientation of IMF B_z .

We note that, despite being widely used in the historical literature, the term “penetration efficiency” is likely inaccurate or, at least, not wholly appropriate. Stemming

70 from earlier studies, such as Cowley (1981), the term implies that the change in the local
 71 field topology is the direct result of the IMF field lines themselves making their way,
 72 or “penetrating”, into the magnetosphere, i.e. through the Dungey Cycle (Dungey, 1961).
 73 The timescale for this process would be several hours, yet more recent results have sug-
 74 gested that a B_y component can be imparted onto closed field lines over significantly shorter
 75 timescales (e.g. Khurana et al., 1996; Tenfjord et al., 2015, 2017) though the issue of tim-
 76 ing remains an open question (e.g. Case et al., 2018, 2020). It is for this reason, that later
 77 studies have tended to refer to the IMF “inducing”, or “transferring”, a B_y component
 78 onto the magnetospheric field lines - particularly in the region of closed field lines.

79 In this study, we extend the historical literature to determine the response of the
 80 inner magnetosphere ($r < 7R_E$) to the IMF B_y component. To date, the effect of the
 81 IMF B_y component on the large-scale local magnetic field in this region, particularly within
 82 $5R_E$, has not yet been statistically documented. As described in Section 2, we utilise a
 83 multi-mission data set spanning 7 years (17 spacecraft years), as well as an empirically
 84 driven magnetic field model, to statistically analyse how the local B_y component changes
 85 as a result of the IMF B_y component. In Section 3, we compare the spacecraft measure-
 86 ments, with a model background field subtracted, to the IMF B_y for a range of differ-
 87 ent IMF conditions and find the average “penetration efficiency” to be 0.33 across the
 88 entire inner magnetosphere.

89 2 Data and Methodology

90 For the purposes of this study, data are used from the Electric and Magnetic Field
 91 Instrument Suite and Integrated Science (EMFISIS) fluxgate magnetometer (Kletzing
 92 et al., 2013), which is housed on board the dual satellite NASA Van Allen Probes (for-
 93 merly Radiation Belt Storm Probe, RBSP) mission (Mauk et al., 2013). The EMFISIS
 94 tri-axial fluxgate magnetometer measures the 3D magnetic field vector at a rate of 64
 95 samples per second. This data set is available in full resolution, or with a downsampled
 96 cadence of both 1 s and 4 s. The following analyses incorporate all available magnetic
 97 field observations from both Van Allen Probes spacecraft spanning the full mission du-
 98 ration, from launch on 30 August 2012, to mission end on 18 October 2019 for RBSP-
 99 A, and 19 July 2019 for RBSP-B.

100 Also included in this study are data from the Japanese geospace exploration project
 101 Arase satellite, formerly the Exploration of energization and Radiation in Geospace satel-
 102 lite (ERG) (Miyoshi, Shinohara, et al., 2018) which launched on 20 December 2016. The
 103 Arase Magnetic Field Experiment (MGF) (Matsuoka et al., 2018) measures the magnetic
 104 field at a sampling rate of 256 vectors per second, but data are also provided at 64 vec-
 105 tors per second and spin (8s) resolution. The accuracy of the MGF data is dependent
 106 upon which sampling mode the instrument is in, with lower accuracy for higher dynamic
 107 ranges. In this study, we utilise Arase MGF data spanning the period from 13 March
 108 2017 to 31 August 2019, with an accuracy of at least ± 1.25 nT. These data are combined
 109 with observations from the Van Allen Probes to provide high levels of data coverage across
 110 all regions of the inner magnetosphere.

111 Due to the statistical nature of the following analyses, and to temporally align the
 112 spacecraft data with upstream IMF conditions, all spacecraft data are resampled to 1
 113 minute resolution. The IMF data are obtained from the high-resolution (1 min) OMNI-
 114 web database (King & Papitashvili, 2005). These data are recorded by several upstream
 115 observers and then time-shifted to the bowshock nose. Although there are inherent un-
 116 certainties in undertaking such a shifting process, especially when the upstream observer
 117 is not close to the Sun-Earth line, the approach is statistically valid (e.g. Mailyan et al.,
 118 2008; Case & Wild, 2012). Since we are investigating the magnetic field in the inner mag-
 119 netosphere, spacecraft data are presented in the solar-magnetic (SM) coordinate system

120 so that they are aligned with Earth’s magnetic dipole. IMF data are presented in the
 121 geocentric solar magnetospheric (GSM) coordinate system.

122 The spatial data coverage of both the Van Allen Probes and Arase missions is pro-
 123 vided in Figure 1 in SM coordinates. Data coverage for Van Allen Probes is shown in
 124 panels a and b, Arase in panels c and d, and the combined data set in panels e and f.
 125 In panels a, c, and e, data coverage is plotted by location in the X and Y plane, and each
 126 bin is $1R_E$ by 1 hour in Magnetic Local Time (MLT) in size. In panels b, d, and f, data
 127 coverage is plotted by location in the XY (i.e. $\sqrt{X^2 + Y^2}$) and Z plane, and the bins are
 128 $1R_E$ square. The bin fill colour represents the total number of 1 min data points con-
 129 tained within it.

130 For both missions, data coverage is approximately homogeneous in MLT, due to
 131 the long duration of the data and the orbital precession of the spacecraft. The greatest
 132 number of observations are available between 5 and 6 R_E for both satellite missions, due
 133 to their similar apogee altitude. The larger orbital inclination of Arase (31°) provides
 134 greater coverage in the Z_{SM} direction than is possible solely from Van Allen Probes ob-
 135 servations (10.2° inclination). We note that the Van Allen Probes mission contributes
 136 significantly more data to this study than the Arase mission simply due to its dual-spacecraft
 137 nature and longer period of operation.

138 2.1 Magnetospheric models

139 In the following analyses, the Van Allen Probes and Arase in situ magnetic field
 140 data are compared against modelled background field values to determine what effect
 141 the IMF B_y component has on the magnetic field in the inner magnetosphere. In this
 142 region, the background field is a radially-dependent combination of an internally-driven
 143 component (i.e. the terrestrial quasi-dipolar field) and an externally-driven component
 144 (i.e. the solar wind/IMF shaped magnetosphere).

145 To determine the internal component of the background field, we utilise the lat-
 146 est version of the International Geomagnetic Reference Field (IGRF 13) (Thébault et
 147 al., 2015). The IGRF is derived from magnetic field data recorded by magnetic obser-
 148 vatories, ground surveys, and low Earth orbiting satellites and is regularly updated to
 149 account for the latest variations in the Earth’s magnetic field. It is independent of any
 150 upstream solar wind or IMF conditions.

151 The externally-driven component of the background field is determined using the
 152 empirically-derived T01 model of the inner magnetosphere (Tsyganenko, 2002a, 2002b).
 153 T01 was developed using in situ observations from a range of spacecraft missions (see
 154 Figure 1 of Tsyganenko (2002b) for mission and temporal coverage) and is driven by a
 155 variety of upstream parameters, including the solar wind speed and the IMF B_y and B_z
 156 components, as well as their time history. We note that the Van Allen Probes and Arase
 157 missions were not part of the T01 empirical data set and so their data are independent
 158 of the modelling data.

159 The IMF B_y component is utilised as a parameter in the T01 model in the calcu-
 160 lation of the IMF clock angle and external magnetic pressure. IMF B_y contributes, for
 161 example, to the determination of the model’s penetration efficiency term - which is clock
 162 angle dependent (Equation 10 in Tsyganenko (2002b)). It is therefore expected that the
 163 effects of the IMF B_y component on the inner magnetosphere would be hidden when com-
 164 paring the in situ data with the model output. As such, we also compare the in situ ob-
 165 servations with a version of T01 in which we set both the instantaneous and historical
 166 IMF B_y to zero. This removes the IMF B_y influence on the modelled B_y field compo-
 167 nent but ensures that other contributions, such as spacecraft location and dipole tilt an-
 168 gle, are accounted for. We note that the external magnetic pressure exerted on the mag-

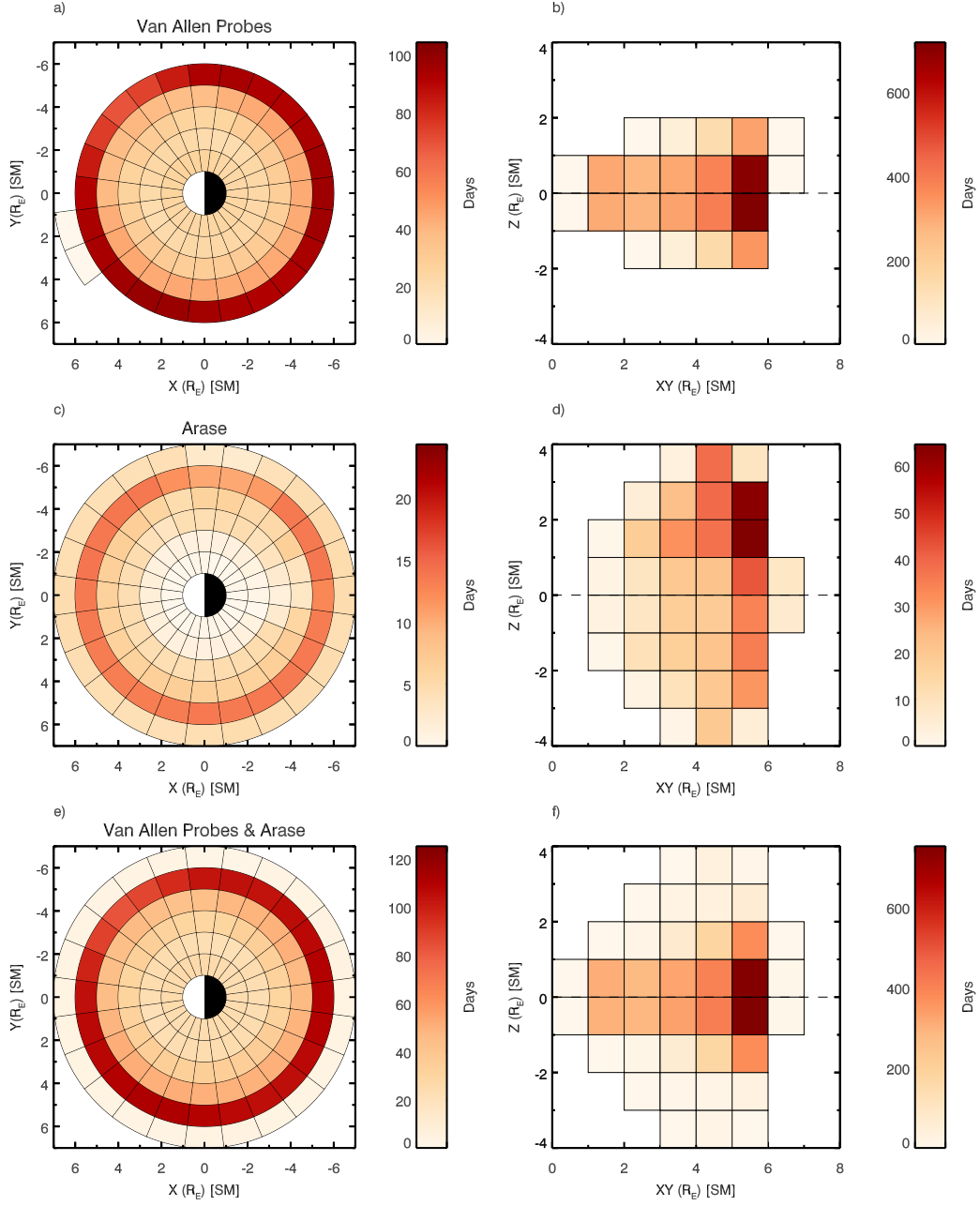


Figure 1. Data coverage for (a and b) Van Allen Probes, (c and d) Arase, and (e and f) both missions combined. Coverage in panels a, c, and e is given in the X-Y plane and bins are $1R_E$ by 1 hour MLT in size. In b, d, and f coverage is in the XY-Z plane and bins are $1R_E$ square in size. Bins are coloured by the number of 1 min resolution data contained within them (1 day = 1,440 data points). Data are in SM coordinates.

169 netosphere (i.e. $\frac{B_t^2}{\mu_0}$, where $B_t = \sqrt{B_y^2 + B_z^2}$) will therefore likely be underestimated,
 170 however, this is a relatively small systematic offset that does not significantly affect the
 171 responses seen (e.g. Tenfjord et al., 2017).

172 In the subsequent results and discussion, “model” is the modelled field calculated
 173 by the addition of the IGRF and T01 field contributions, including IMF B_y as a driver,
 174 and $B_{y(mod)}$ is the y-component of this field. “Model*” is the modelled field calculated
 175 by the addition of the IGRF and T01, with IMF $B_y = 0$, and $B_{y(mod*)}$ is the y-component
 176 of this field. The field measured by the spacecraft is referred to as the “observed” field
 177 and $B_{y(obs)}$ denotes the y-component of this field. Although not the primary aim of this
 178 study, comparing the “observed” data to “model” allows us to verify that the combina-
 179 tion of models we use is working well for our data intervals.

180 The spacecraft data are also sorted by hemisphere, i.e. either side of the neutral
 181 sheet which separates the oppositely directed magnetic lobes. Since the neutral sheet is
 182 not necessarily located on the $Z_{SM} = 0$ plane, we use both the spacecraft location and
 183 the in situ measured field to determine which hemisphere the spacecraft is located in at
 184 any given time. Data are defined as being sampled from the Northern Hemisphere when
 185 $Z_{SM} > 0 R_E$ and $B_i < 0$, where $B_i = (B_x \cos \theta + B_y \sin \theta)$ and $\theta = \tan^{-1} \left(\frac{Y_{SM}}{X_{SM}} \right)$.
 186 Conversely, data are defined as being sampled from the Southern Hemisphere when $Z_{SM} <$
 187 $0 R_E$ and $B_i > 0$. Given the reasonably steady nature of the solar wind (e.g. Milan
 188 et al., 2010), the median IMF B_y is calculated for each spacecraft data point simply us-
 189 ing the preceding 30 min of IMF B_y data, neglecting any propagation time from the bow-
 190 shock to the magnetopause or magnetospheric response time.

191 3 Results

192 Figure 2 shows data recorded in the Northern Hemisphere. In the top row, are the
 193 median $B_{y(obs)}$ values per bin for (left) IMF $B_y < -2$ nT, (centre) $|B_y| < 1$ nT, and
 194 (right) $B_y > 2$ nT. As with Figure 1, the data bins are $1R_E$ in the radial direction and
 195 1 hour in MLT in size. The colour of the bin represents the median value.

196 In the middle row of Figure 2 are the median $B_{y(obs)} - B_{y(mod*)}$ values. The IMF
 197 $B_y < -2$ nT panel is clearly dominated by blue coloured bins, i.e. $B_{y(mod*)} > B_{y(obs)}$.
 198 By contrast, the IMF $B_y > 2$ nT is predominantly red, i.e. $B_{y(obs)} > B_{y(mod*)}$, but
 199 with a sizeable collection of blue coloured bins particularly around the dusk sector. We
 200 note too that the IMF $|B_y| < 1$ nT state appears to be dominated by blue bins, sug-
 201 gesting an offset in which model* systematically overestimates the local B_y field. The
 202 median absolute relative percentage of the IMF $B_y = 0$ offset to the $B_{y(obs)} - B_{y(mod*)}$
 203 value for the two non-zero states is 45.0% - though it does vary across MLT and radial
 204 distances. To remove this systematic offset, in the bottom row of Figure 2, we plot the
 205 median $B_{y(obs)} - B_{y(mod*)}$ minus the corresponding offset observed for the IMF $|B_y| <$
 206 1 nT state. In both the IMF $B_y > 2$ nT and $B_y < -2$ nT cases, the previously men-
 207 tioned trends become clearer across almost all radial and MLT bins once this offset is
 208 removed.

209 Data recorded in the Southern Hemisphere are plotted in Figure 3, in the same for-
 210 mat as Figure 2. We find a similar response in the Southern Hemisphere as in the North-
 211 ern Hemisphere, with a clear dependence of the observed B_y component on the IMF B_y
 212 component.

213 MLT sector and hemisphere dependencies are also investigated, with results shown
 214 in Figure 4. Plotted are (panels a and d) the median $B_{y(obs)}$ values, (b and e) median
 215 $B_{y(obs)} - B_{y(mod*)}$, and (c and f) $B_{y(obs)} - B_{y(mod)}$ values as a function of their respec-
 216 tive 30 min (a to c) IMF B_y and (d to f) clock angle averages. To determine if the re-
 217 sponse of the observed field is different between hemispheres, or between the dusk and

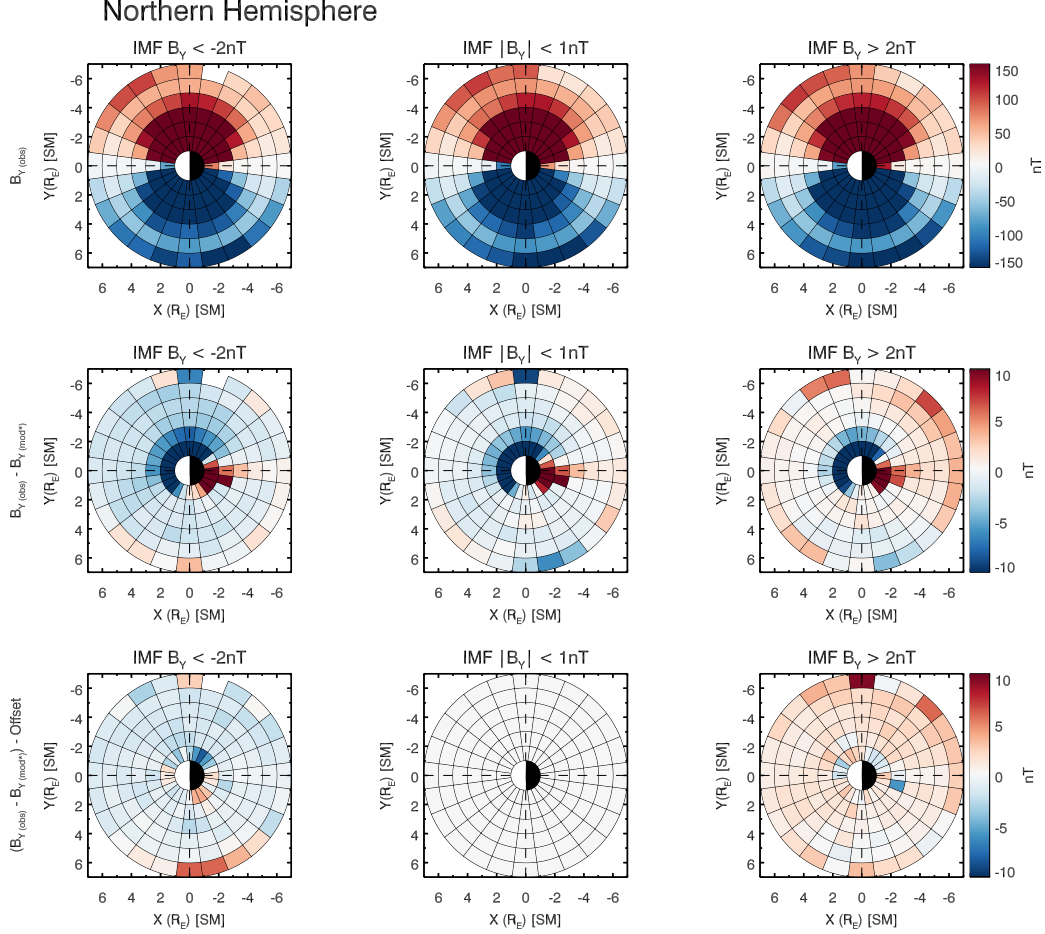


Figure 2. Van Allen Probes and Arase data sampled from the Northern Hemisphere are shown for (left) IMF $B_y < -2$ nT, (centre) IMF $|B_y| < 1$ nT, and (right) IMF $B_y > 2$ nT states. (Top) Data bins are coloured by median local B_y , (middle) the median difference between the local B_y and the modelled B_y value, and (bottom) the median difference between the local B_y and the modelled B_y value with the corresponding median values from the IMF $|B_y| < 1$ state further subtracted. Data bins span $1R_E$ in the radial direction and 1 hour in MLT.

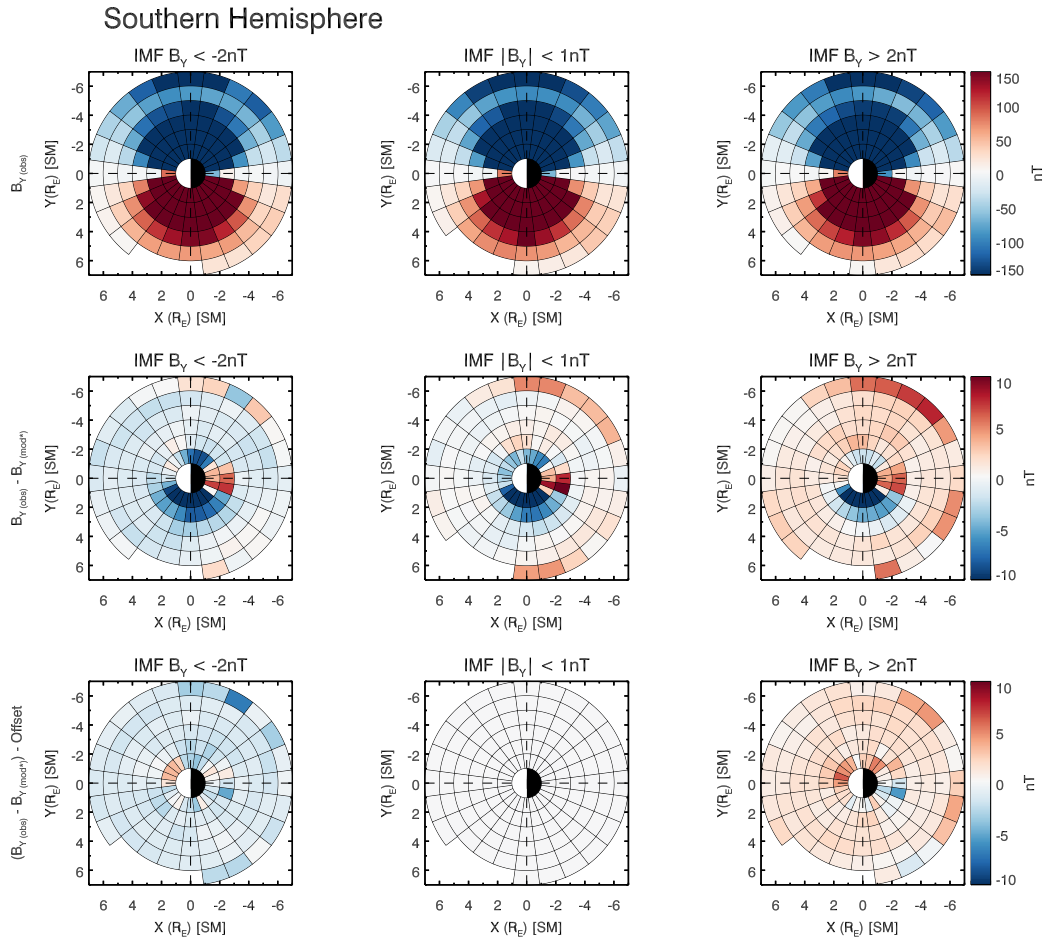


Figure 3. Van Allen Probes and Arase data sampled from the Southern Hemisphere are presented in the same format as Figure 2.

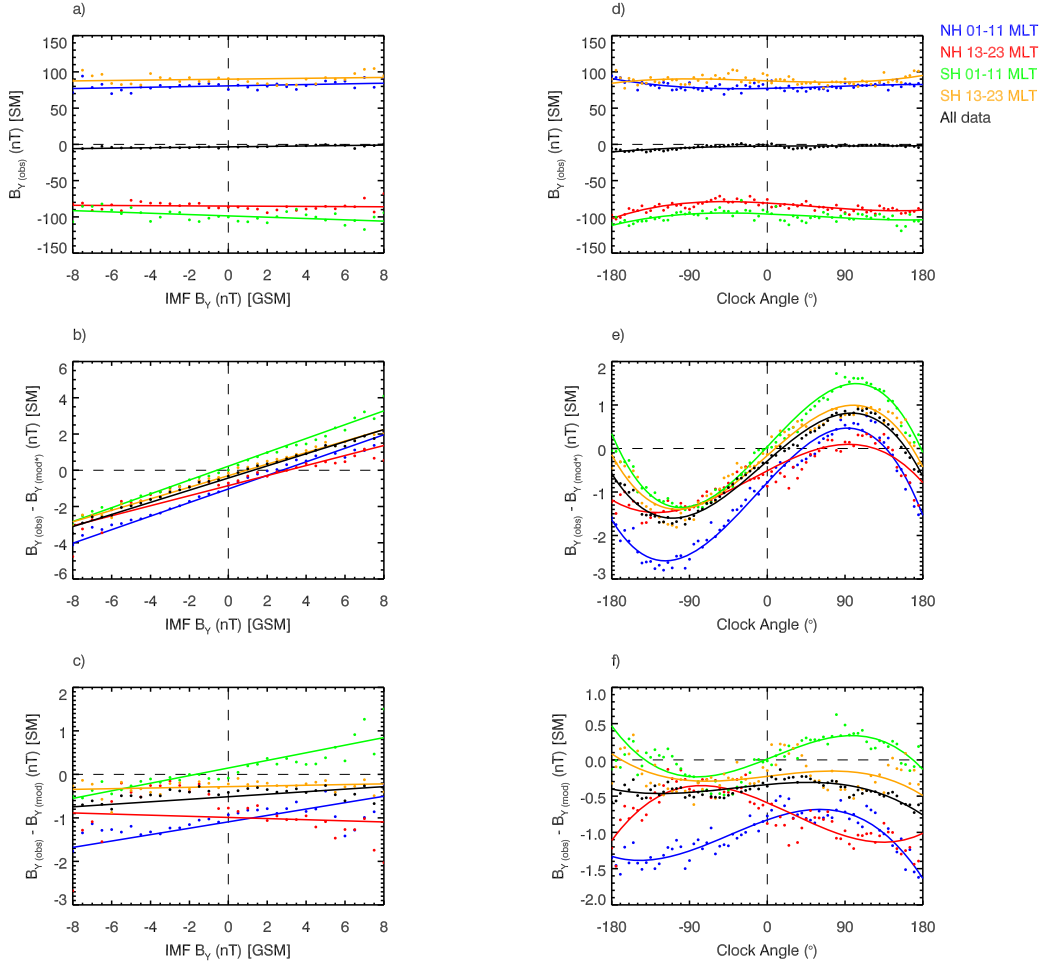


Figure 4. Plotted in (a) are the median $B_{y(obs)}$ values for specific local time and hemispheric sectors, as a function of the upstream IMF B_y and (d) clock angle. In (b and e) the medians of the $B_{y(obs)} - B_{y(mod*)}$ values are shown whilst in (c and f) the medians of the $B_{y(obs)} - B_{y(mod)}$ values are shown. In all panels, the medians from data sampled in the Northern Hemisphere between 01 and 11 MLT are plotted in blue, and between 13 and 23 MLT in red. Medians from data sampled from the Southern Hemisphere between 01 and 11 MLT are plotted in green and between 13 and 23 MLT in orange. The median of all data is plotted in black.

218 dawn sectors, data are separated into the following regions: Northern Hemisphere 01-
 219 11 MLT (blue) and 13-23 MLT (red), and Southern Hemisphere 01-11 MLT (green) and
 220 13-23 MLT (orange). The medians of all regions combined (i.e. all data) are plotted in
 221 black. Additionally, for every region, in each panel, a line of best fit is plotted. For the
 222 IMF B_y plots (a to c) the line of best fit is linear, for the clock angle (d to f) plots the
 223 line of best fit is a third order polynomial.

224 In Figure 4, panels a and d, it appears that $B_{y(obs)}$ does not respond to the IMF
 225 B_y component. As previously mentioned, however, this is simply because the background
 226 field is much larger than the IMF B_y component. When we subtract the background model*
 227 field, in panels b and e, the relationship becomes clear.

228 As shown in panel b, there is a clear linear dependence between the IMF B_y component
 229 and $B_{y(obs)} - B_{y(mod^*)}$. All MLT regions exhibit a similar response, with the line
 230 of best fit equation for all data (black line) being: $B_{y(obs)} - B_{y(mod^*)} = 0.33 \times \text{IMF } B_y -$
 231 0.41 nT . We note that the negative intercept of this line of best fit is consistent with the
 232 negative (blue) offset observed in the middle panel of Figure 2.

233 In Figure 4e, third order polynomial fits between the IMF clock angle and $B_{y(obs)} -$
 234 $B_{y(mod^*)}$ are shown. Again these fits are broadly similar for all MLT regions. The turning
 235 points of the various fits are all offset from $\theta = \pm 90^\circ$ (i.e. IMF $B_z = 0$). For the
 236 all data medians (black line), the maximum and minimum occur at $\theta = 97^\circ$ and $\theta =$
 237 -109° respectively. Both of these turning points demonstrate that whilst the clock angle
 238 must be dominated by the IMF B_y component contribution, it must also contain a
 239 relatively small southward B_z component to maximise the influence of the IMF B_y component
 240 on the inner magnetosphere.

241 We note that the absolute difference between the maximum and minimum clock
 242 angles and $|\theta| = 90^\circ$ is 7° and 19° respectively. This indicates that there is a small asym-
 243 metry between the required relative contribution of IMF B_y and B_z for the two IMF B_y
 244 orientations. This result suggests that for IMF B_y to be most effective in the inner mag-
 245 netosphere for $B_y < 0$, a more strongly negative IMF B_z component is required com-
 246 pared to when IMF $B_y > 0$.

247 In Figure 4, panels c and f, $B_{y(obs)} - B_{y(mod)}$ is compared against the IMF B_y com-
 248 ponent and clock angle. There is no clear trend in either panel that is apparent across
 249 all MLT sectors, and we note that the residuals are small - generally less than 1nT.

250 To investigate any radial dependencies in the data, we split the data by location
 251 in MLT and then bin by radial distance from the Earth. One representative example of
 252 this binning is shown in Figure 5, where data are sampled from the Northern Hemisphere
 253 in the 01-11 MLT sector. The lines of best fit plotted in the figure are the medians of
 254 the data from this MLT sector, binned by radial distance from the Earth.

255 The results in Figure 5 are very similar to those in Figure 4. There is a clear lin-
 256 ear response at almost all radial distances when $B_{y(obs)} - B_{y(mod^*)}$ is plotted against
 257 IMF B_y , and a third order polynomial response when plotted against IMF clock angle.
 258 In panel b, the gradients of the IMF B_y linear fits are broadly similar as with the MLT
 259 sectors (~ 0.3). The third order polynomial fits to the clock angle (panel e) follow sim-
 260 ilar patterns as before with the maxima and minima, for all fits, occurring at $\theta \sim 95^\circ$
 261 and $\theta \sim -110^\circ$ respectively. We note the $6 \leq r < 7R_E$ bin is an exception to this
 262 which we attribute to the relatively small number of data points in this bin - as appa-
 263 rent in Figure 1e.

264 To determine the degree to which the IMF B_y influences the observed B_y compo-
 265 nent across the whole of the inner magnetosphere, we compute linear lines of best fit for
 266 $B_{y(obs)} - B_{y(mod^*)}$, and $B_{y(obs)} - B_{y(mod)}$, as a function of IMF B_y for all MLT-r sec-
 267 tors. The gradients of these fits, are plotted in Figure 6. Data is recorded in (panels a
 268 and d) the Northern Hemisphere, (b and e) the Southern Hemisphere and (c and f) both
 269 hemispheres combined. The gradients of the fits are computed separately for data in each
 270 $1R_E$ and 1 hr MLT bin. The color of the bins represents the gradient of the fits for the
 271 data in that bin. Gray bins indicate limited data (where there was not data for every
 272 IMF B_y bin) or poor fits (where the unreduced chi-square goodness-of-fit statistic was
 273 greater than 1).

274 Panels a-c show the fit gradients range from $\sim 0.2-0.5$ throughout the inner mag-
 275 netosphere, though there appears to be no particular pattern to this distribution and there
 276 is little discernible difference between hemispheres. The gray bins are predominantly due
 277 to limited data in the outer radial bins (i.e. $6 \leq r < 7R_E$). The result is much more

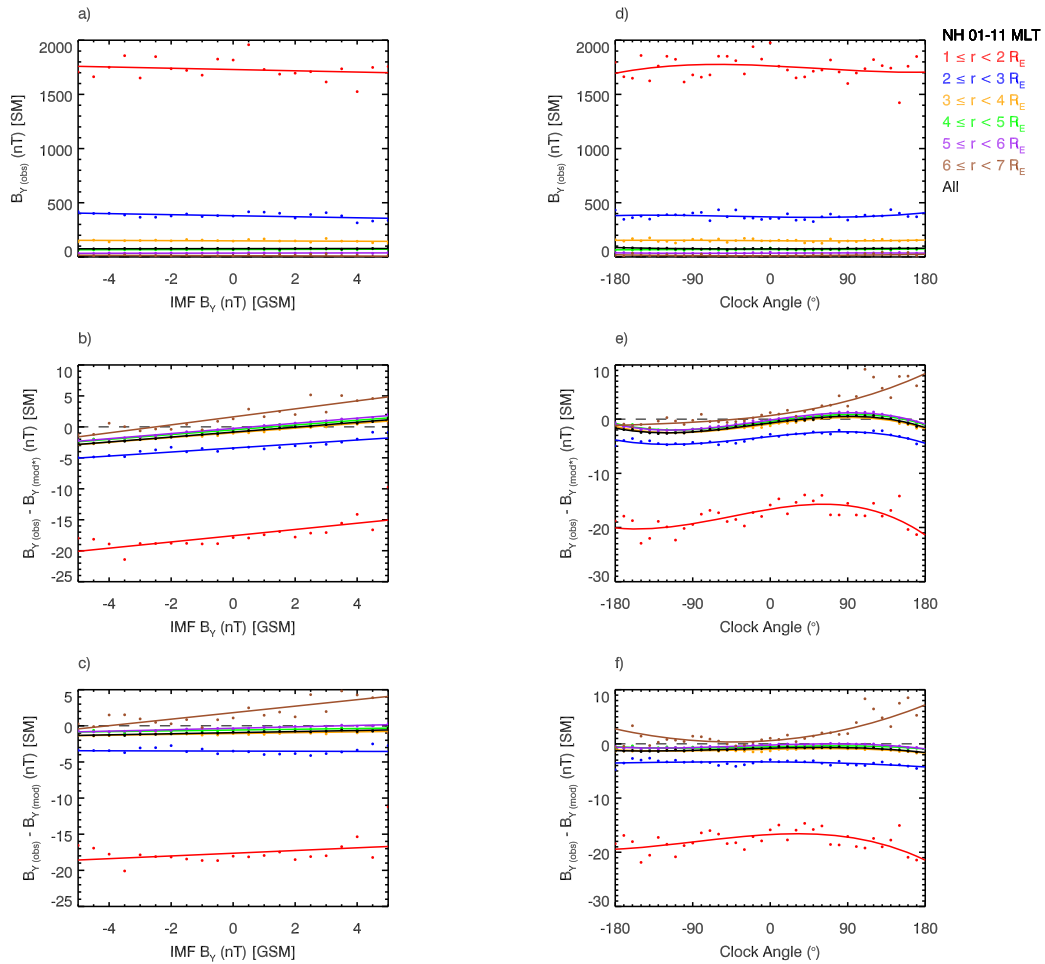


Figure 5. In a similar format as Figure 4 but with the medians of data by radial distance, for the Northern Hemisphere 01-11 MLT sector, as a function of (panels a-c) IMF B_y and (panels d-f) clock angle.

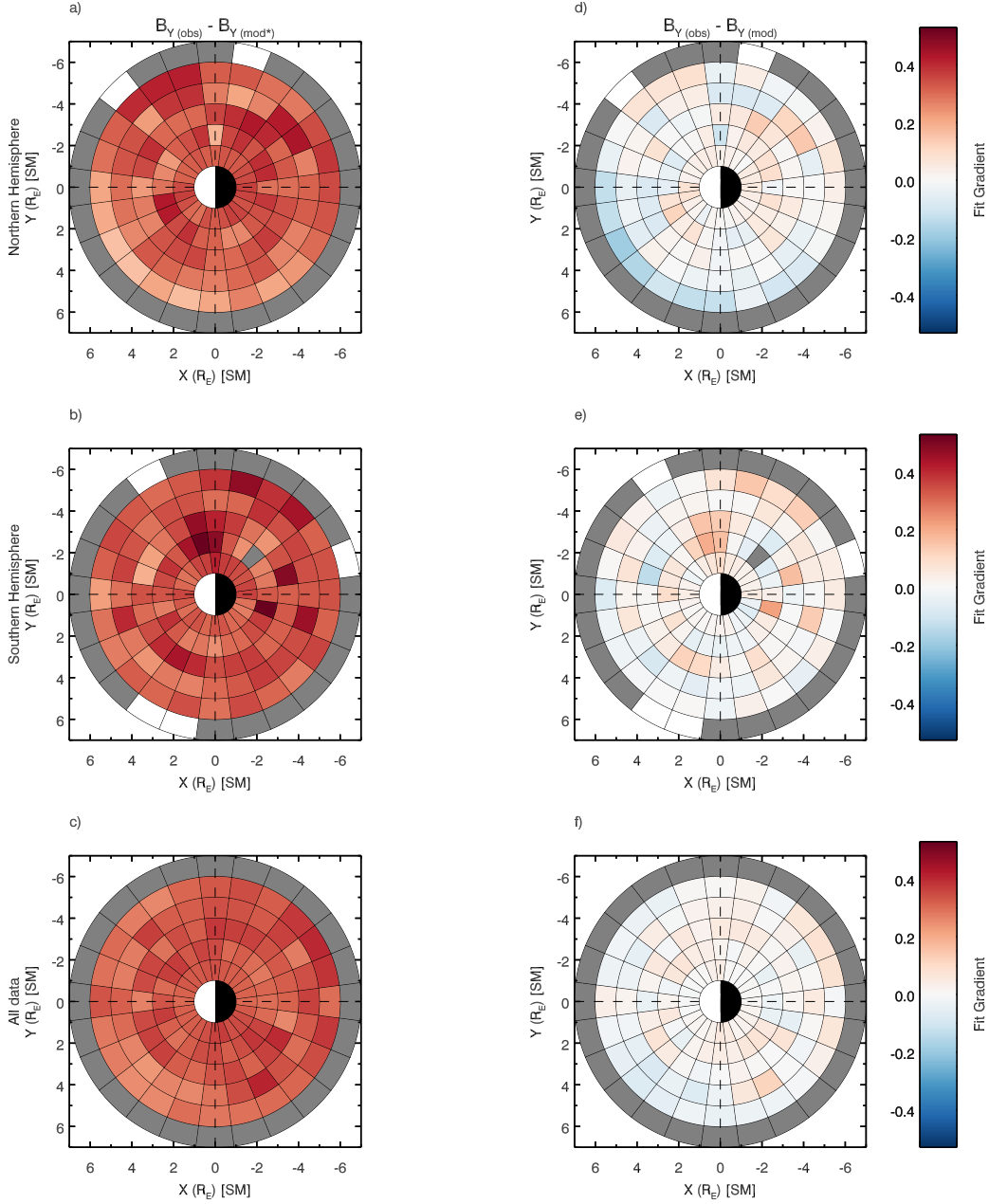


Figure 6. Plotted in panels a to c are the gradients of the linear line of best fits for IMF B_y against $B_{y(obs)} - B_{y(mod*)}$ and in panels d to f for $B_{y(obs)} - B_{y(mod)}$. Data in panels a and d are recorded in the Northern Hemisphere, b and e in the Southern Hemisphere and both hemispheres combined in panels c and f. The gradients of the fits are computed for data in $1R_E$ and 1 hr MLT bins. The color of the bins represents the gradient of the fits for the data in that bin. Gray bins indicate limited data or poor fits.

278 mixed for panels d-f, with gradients ranging between ± 0.2 , though again there is no par-
 279 ticular pattern to this distribution.

280 Since Figures 4 and 5 demonstrate that $|B_{y(obs)} - B_{y(mod^*)}|$ is largest when $|\theta| \sim$
 281 $90 - 110^\circ$, we have also performed the same analyses as in Figure 6 for two clock an-
 282 gle dependent states. Specifically, we plot the distribution of gradients for (a) “all data”,
 283 (b) $90^\circ < |\theta| \leq 135^\circ$, and (c) “other” (i.e. $|\theta| \leq 90^\circ$ and $|\theta| > 135^\circ$) in Figure 7.

284 Figure 7 clearly shows that the distributions for the line of best fit gradients are
 285 dependent upon clock angle. The median value is 0.33 for all data, 0.4 for $90^\circ < |\theta| \leq$
 286 135° , and 0.3 for “other”.

287 4 Discussion

288 In this study we have collated magnetic field data from two spacecraft missions in
 289 the inner magnetosphere, namely the Van Allen Probes and Arase. Utilising the IGRF
 290 13 and T01 magnetic field models to determine the “background field level”, we have demon-
 291 strated how the IMF B_y component affects the y-component of the magnetic field in the
 292 inner magnetosphere.

293 As shown in Figure 1, our data are recorded in the $R_{XY} < 7R_E$ and $|Z| < 4R_E$
 294 region, in SM coordinates. The Van Allen Probes and Arase missions provide unparal-
 295 leled coverage in this region, allowing us to undertake comprehensive statistical analy-
 296 ses of the local magnetic field in the inner magnetosphere with respect to the upstream
 297 IMF B_y component.

298 In the top row of Figure 2, we show the median observed B_y component for three
 299 IMF B_y states: IMF $B_y < -2$ nT, IMF $|B_y| < 1$ nT, and IMF $B_y > 2$ nT. Unsurpris-
 300 ingly, since the total field strength in this region is several orders of magnitude larger
 301 than the IMF, there is no discernible difference between the IMF B_y states when the data
 302 is presented this way. However, when the background field ($B_{y(mod^*)}$) is subtracted, as
 303 in the middle row of Figures 2 and 3, the response to the IMF B_y component becomes
 304 clear. There does, however, appear to be some asymmetry in the data. The IMF $B_y <$
 305 -2 nT shows a much clearer response than the IMF $B_y > 2$ nT state and the IMF $|B_y| <$
 306 1 nT state appears to be more like a weakened version of the IMF $B_y < -2$ nT state,
 307 rather than a true “neutral” (or zero) state. These results suggest that model* B_y is over-
 308 estimating the y-component of the magnetic field in all cases. The results from Figure 3
 309 are broadly similar to their counterparts in Figure 2, indicating there is little-to-no dis-
 310 cernible difference between the two hemispheres.

311 In Figures 4 and 5 we plot the median $B_{y(obs)}$, $B_{y(obs)} - B_{y(mod^*)}$, and $B_{y(obs)} -$
 312 $B_{y(mod)}$ as a function of (a-c) IMF B_y and (d-f) IMF clock angle. In Figure 4 the data
 313 are plotted by their location in MLT and in Figure 5 by their radial location. The re-
 314 sults of these two figures are similar, and so are discussed together.

315 In panels a to c, the data are plotted as a function of IMF B_y in the range of ± 6 nT.
 316 We note that outside this range the amount of data drops off significantly resulting in
 317 poor fits (i.e. a large chi-square goodness-of-fit statistic). Once the background field is
 318 subtracted (panel b), the effect of the IMF B_y component becomes clear. Using a lin-
 319 ear least squares fit, we find a direct relationship between the IMF B_y and the $B_{y(obs)} -$
 320 $B_{y(mod^*)}$ residual. The gradients, or “penetration efficiencies”, are similar for all MLT
 321 and r regions, averaging around 0.33. Whilst the the line of best fit offsets do vary, even
 322 the largest offset (Figure 5b) is, when normalized to the strength of the background field,
 323 small. Though it is interesting to note that almost all offsets are negative, even when
 324 taking into account the IMF B_y component in the model (i.e. $B_{y(obs)} - B_{y(mod)}$) - which
 325 is consistent with the slightly negative local B_y state observed for IMF $|B_y| < 1$ nT in
 326 Figures 2 and 3.

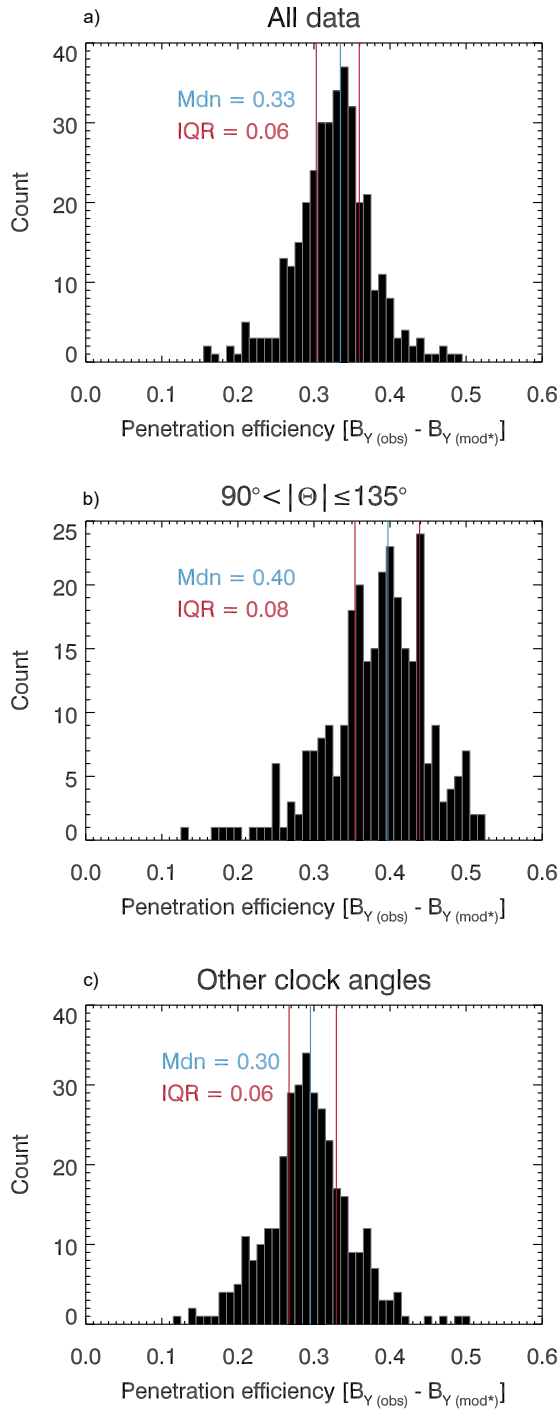


Figure 7. The distribution of linear fit gradients is shown for (a) “all data”, (b) $90^\circ < |\theta| \leq 135^\circ$ and (c) “other” clock angles. The median (Mdn) and interquartile range (IQR) are also shown for each distribution.

327 In Figures 4 and 5 panels (d-f), the data are plotted as a function of clock angle.
 328 Based on the assumption that the fits should have a maximum amplitude when IMF B_y
 329 is dominant and zero amplitude when no IMF B_y is present, a third order polynomial
 330 is used to fit the data. A third order polynomial, unlike a sine function for example, al-
 331 lows for an asymmetry in the turning points of the fit, which is particularly evident in
 332 panel e of both figures. In Figure 4, for example, the maximum turning point is located
 333 at $\theta = 97^\circ$ and the minimum turning point at $\theta = -109^\circ$. The clock angles for both
 334 turning points occur when the IMF $|B_y|$ component is several times larger than the IMF
 335 $|B_z|$ component, but the IMF B_z component is non-zero and negative. The maximum
 336 and minimum of the fits do not occur at the same $|\theta|$, which demonstrates that the ra-
 337 tio between the IMF B_y and B_z components required for maximum amplitude is differ-
 338 ent for the two opposite IMF B_y directions. This result may indicate that one orienta-
 339 tion of the IMF B_y component more readily facilitates reconnection than the other or
 340 that the topology of newly opened flux increases/decreases the efficiency for which the
 341 B_y component is transferred into the inner magnetosphere. We note, however, that these
 342 differences are small and are the maximum and minimum of the fits, rather than the data
 343 themselves, and so may be prone to fitting error. Further investigation into this observed
 344 discrepancy, perhaps through magnetohydrodynamic modelling, therefore seems warranted.

345 When comparing hourly averaged IMF and observed B_y components in the $X_{GSM} \sim$
 346 -20 to $-30R_E$ region, Fairfield (1979) found a linear relation of $\Delta B_y(\text{tail}) = 0.13 \times$
 347 $B_y(\text{IMF}) - 0.30\text{nT}$. This compares to our result, as shown in Figure 4 for all data (black
 348 line), of $B_{y(\text{obs})} - B_{y(\text{mod}^*)} = 0.33 \times \text{IMF} B_y - 0.41\text{nT}$. Of course, our data are recorded
 349 in a much different region of the magnetosphere than the IMP 6 spacecraft used by Fairfield
 350 (1979) and has also had other non-IMF B_y related effects removed from it through use
 351 of the T01 model. Cowley (1981) noted that, because the Fairfield (1979) result was found
 352 in both the tail lobes and the plasma sheet, it directly implied the existence of asym-
 353 metries on closed field lines. Indeed, all data used in this present study are within $7R_E$,
 354 i.e. on closed field lines. Numerous studies that followed on from the Fairfield (1979) in-
 355 vestigation have found the “penetration efficiency”, i.e. the gradient of the lines of best
 356 fit, to vary depending on the region of the magnetosphere being studied and IMF con-
 357 ditions (e.g. Fairfield, 1979; Cowley & Hughes, 1983; Lui, 1984; Nagai, 1987; Kaymaz
 358 et al., 1994; Wing et al., 1995; Petrukovich, 2009; Cao et al., 2014). For example, in the
 359 T01 model, which is used throughout this study, the penetration efficiency ranges from
 360 0.068 for northward IMF to 0.622 for southward, however, it is not location dependent
 361 (Tsyganenko, 2002b). In recent work by Tsyganenko and Andreeva (2020), modelling
 362 of the neighbouring regions to the one in our study found similar efficiencies of between
 363 0.2 and 0.4, with the larger efficiencies occurring during southward IMF.

364 The general relationship of $\Delta B_{y(\text{obs})} \sim 0.33 \times \text{IMF} B_y$ holds throughout the in-
 365 ner magnetosphere. There is, of course, some variation in the gradient of the relation by
 366 MLT sector and by radial distance, as can be seen in Figures 4 and 5. However, the me-
 367 dian gradient for the 1 hour MLT by $1 R_E$ bins in Figure 6 is 0.33, with an interquar-
 368 tile range of 0.07, suggesting the general trend holds throughout this region. Again, this
 369 is consistent with recent modelling work, e.g. Figure 4 in Tsyganenko and Andreeva (2020).

370 We note that southward IMF has resulted in a higher penetration efficiency in past
 371 studies and, as discussed, we too see this effect in Figures 4e and 5e. We have, therefore,
 372 also investigated the effect of southward IMF on our penetration efficiencies. Shown in
 373 Figure 7 are the distributions of the penetration efficiency for three clock angle states:
 374 “all data”, $90^\circ < |\theta| \leq 135^\circ$, and “other”. The median penetration efficiencies for these
 375 states are 0.33, 0.40, and 0.30, respectively. This result demonstrates that the penetra-
 376 tion is higher when the IMF B_y is dominant but accompanied by a negative B_z . This,
 377 presumably, is the result of southward IMF driving a larger dayside reconnection rate
 378 which, in turn, increases the amount of flux being transferred from the IMF into the mag-
 379 netosphere. Given that the difference between the median values presented is quite small,

we compare the two sample population distributions, using the statistical z-test, finding that difference between the two distributions is highly significant.

Our analyses have also allowed us to compare the in situ magnetic field with the combined modelling of IGRF 13 and T01. Woodfield et al. (2007) compared T01 with two years of perigee Cluster data ($\sim 4R_E$) and found the model performed very well in a global sense. Although such testing was not the main aim of this study, our results agree with this assessment. The results of the analyses undertaken, particularly those presented in Figures 4 and 5 (panels c and f), suggest that the T01 model accurately reflects the impact of the IMF B_y on the observed B_y component in the inner magnetosphere, i.e. the line of best fit gradients. Although the offsets of the lines of best fit may sometimes appear large, they represent a small fraction of the total background magnetic field in this region. We note that we are able to attribute this accurate IMF B_y response solely to the T01 model since the IGRF model does not contain any solar wind/IMF inputs.

In this study, the issue of timing, i.e. how long it takes the inner magnetosphere to respond to, and reconfigure based on, the IMF B_y component, has not been investigated. Instead all spacecraft data were associated with the preceding 30 min average of the IMF B_y component. Whilst the response to the IMF B_y component was clearly seen on this timescale, this does not necessarily mean that it takes 30 min or less for the IMF B_y component to influence the inner magnetosphere. The IMF B_y component tends to have a long auto-correlation length (e.g. Milan et al., 2010) and so the IMF B_y may have been stable for much longer than the averaging period used. Additionally, it does not mean that the system has completely reconfigured in this time, and so we expect our results include a combination of fully reconfigured states as well as newly responding states. We note that work by Tenfjord et al. (2015, 2017), who found the inner magnetosphere responded to changes in IMF B_y orientation on timescales of ~ 30 min but took longer to fully reconfigure to the new B_y state. Additionally, this was undertaken using GOES data recorded at geosynchronous orbit ($r \sim 6.6R_E$). It would therefore be a worthwhile exercise investigate the issue of timing using Van Allen Probes and Arase data to determine if their results hold closer to the Earth. Such future work is planned by the authors.

5 Conclusions

Utilising 7 years (17 spacecraft years) of data from two spacecraft missions, namely Van Allen Probes and Arase, we have rigorously investigated the effect of the IMF B_y component on the inner magnetosphere. We have shown that IMF B_y influences the local field in both hemispheres, all radial distances, and all MLT sectors.

The response of the inner magnetosphere to the IMF B_y component scales linearly in the IMF range analysed ($-6 \leq \text{IMF } B_y \leq +6\text{nT}$). The “penetration efficiency”, i.e. the fraction of the IMF B_y component that is imparted onto the background inner magnetospheric field, is largely consistent throughout the inner magnetosphere at ~ 0.33 . This result is consistent with previous studies near this region e.g. Tsyganenko and Andreeva (2020).

The penetration efficiency was found to be clock angle dependent, specifically the maximum efficiency is observed when the clock angle is dominated by the B_y component but also contains a negative B_z component. Again this is consistent with previous studies from other regions of the magnetosphere. The median penetration efficiency increased to 0.4 during favourable conditions ($90^\circ < |\theta| \leq 135^\circ$) and dropped to 0.3 during unfavourable conditions.

Additionally, we have found that, in a statistical sense, the Tsyganenko (2002a, 2002b) model, when combined with the IGRF 13 model (Thébault et al., 2015), accounts for the IMF B_y effect well in the inner magnetosphere.

Acknowledgments

Van Allen Probes EMFISIS data may be obtained from <http://emfisis.physics.uiowa.edu/data/index>. Science data of the ERG (Arase) satellite were obtained from the ERG Science Center operated by ISAS/JAXA and ISEE/Nagoya University (<https://ergsc.isee.nagoya-u.ac.jp/index.shtml.en> (Miyoshi, Hori, et al., 2018)). The present study analyzed MGF-L2 v03.03 data (<http://doi.org/10.34515/DATA.ERG-06000>) and Orbit L3 v02 data. The authors gratefully acknowledge both instrument teams for the collection and production of high quality science data.

The IGRF 13 and T01 field values were computed using the IDL Geopack DLM (v10.6) (<http://ampere.jhuapl.edu/code/idl.geopack.html>).

NAC and AG were supported during this study by STFC grant number ST/R000816/1. DPH performed work under the support of JHU/APL contract number 921647 under NASA Prime contract number NAS5-01072, and JHU/APL contract number 131802 under NASA prime contract number NNN06AA01C. YM was supported during this study by JSPS-KAKENHI grants 15H05815, 16H06286, and 20H01959.

References

- Andreeva, V. A., & Tsyganenko, N. A. (2016). Reconstructing the magnetosphere from data using radial basis functions. *Journal of Geophysical Research: Space Physics*, *121*(3), 2249-2263. doi: 10.1002/2015JA022242
- Cao, J., Duan, A., Dunlop, M., Wei, X., & Cai, C. (2014). Dependence of IMF By penetration into the neutral sheet on IMF Bz and geomagnetic activity. *Journal of Geophysical Research: Space Physics*, *119*(7), 5279-5285. doi: 10.1002/2014JA019827
- Case, N. A., Grocott, A., Fear, R. C., Haaland, S., & Lane, J. H. (2020). Convection in the magnetosphere-ionosphere system: A multimission survey of its response to imf by reversals. *Journal of Geophysical Research: Space Physics*, *125*(10), e2019JA027541. doi: 10.1029/2019JA027541
- Case, N. A., Grocott, A., Haaland, S., Martin, C., & Nagai, T. (2018). Response of earth's neutral sheet to reversals in the IMF By component. *Journal of Geophysical Research: Space Physics*, *123*(10), 8206-8218. doi: 10.1029/2018JA025712
- Case, N. A., & Wild, J. A. (2012). A statistical comparison of solar wind propagation delays derived from multispacecraft techniques. *J. Geophys. Res.*, *117*(A2). doi: 10.1029/2011JA016946
- Cowley, S. (1981). Magnetospheric asymmetries associated with the y-component of the IMF. *Planetary and Space Science*, *29*(1), 79 - 96. doi: 10.1016/0032-0633(81)90141-0
- Cowley, S., & Hughes, W. (1983). Observation of an IMF sector effect in the Y magnetic field component at geostationary orbit. *Planetary and Space Science*, *31*(1), 73 - 90. doi: 10.1016/0032-0633(83)90032-6
- Dungey, J. W. (1961). Interplanetary magnetic field and the auroral zones. *Phys. Rev. Lett.*, *6*(2), 47-48.
- Fairfield, D. H. (1979). On the average configuraton of the geomagnetic tail. *Journal of Geophysical Research: Space Physics*, *84*(A5), 1950-1958. doi: 10.1029/JA084iA05p01950
- Kaymaz, Z., Siscoe, G. L., Luhmann, J. G., Lepping, R. P., & Russell, C. T. (1994). Interplanetary magnetic field control of magnetotail magnetic field geometry: Imp 8 observations. *Journal of Geophysical Research: Space Physics*, *99*(A6), 11113-11126. doi: 10.1029/94JA00300
- Khurana, K. K., Walker, R. J., & Ogino, T. (1996). Magnetospheric convection in the presence of interplanetary magnetic field by : A conceptual model and sim-

- 481 ulations. *Journal of Geophysical Research: Space Physics*, *101*(A3), 4907-4916.
482 doi: 10.1029/95JA03673
- 483 King, J. H., & Papitashvili, N. E. (2005). Solar wind spatial scales in and compar-
484 isons of hourly Wind and ACE plasma and magnetic field data. *Journal of*
485 *Geophysical Research: Space Physics*, *110*(A2). doi: 10.1029/2004JA010649
- 486 Kletzing, C. A., Kurth, W. S., Acuna, M., MacDowall, R. J., Torbert, R. B.,
487 Averkamp, T., . . . Tyler, J. (2013). The electric and magnetic field instrument
488 suite and integrated science (EMFISIS) on RBSP. *Space Science Reviews*,
489 127181. doi: 10.1007/s1121401399936
- 490 Lui, A. T. Y. (1984). Characteristics of the cross-tail current in the earth's magne-
491 totail. In *Magnetospheric currents* (p. 158-170). American Geophysical Union
492 (AGU). doi: 10.1029/GM028p0158
- 493 Mailyan, B., Munteanu, C., & Haaland, S. (2008). What is the best method to cal-
494 culate the solar wind propagation delay? *Annales Geophysicae*, *26*(8), 2383–
495 2394. doi: 10.5194/angeo-26-2383-2008
- 496 Matsuoka, A., Teramoto, M., Nomura, R., Nosé, M., Fujimoto, A., Tanaka, Y., . . .
497 Shinohara, I. (2018). The Arase (ERG) magnetic field investigation. *Earth,*
498 *Planets and Space*, *70*(1), 43. doi: 10.1186/s40623-018-0800-1
- 499 Mauk, B. H., Fox, N. J., Kanekal, S. G., Kessel, R. L., Sibeck, D. G., & Ukhorskiy,
500 A. (2013). Science objectives and rationale for the radiation belt storm
501 probes mission. *Space Science Reviews*, *179*(1), 3–27. doi: 10.1007/
502 s11214-012-9908-y
- 503 Milan, S. E., Grocott, A., & Hubert, B. (2010). A superposed epoch analysis of au-
504 roral evolution during substorms: Local time of onset region. *Journal of Geo-*
505 *physical Research: Space Physics*, *115*(A5). doi: 10.1029/2010JA015663
- 506 Miyoshi, Y., Hori, T., Shoji, M., Teramoto, M., Chang, T. F., Matsuda, S., . . . Shi-
507 nohara, I. (2018). The ERG science center. *Earth, Planets and Space*, *70*. doi:
508 10.1186/s40623-018-0867-8
- 509 Miyoshi, Y., Shinohara, I., Takashima, T., Asamura, K., Higashio, N., Mitani, T., . . .
510 Seki, K. (2018). Geospace exploration project ERG. *Earth, Planets and Space*,
511 *70*. doi: 10.1186/s40623-018-0862-0
- 512 Nagai, T. (1987). Interplanetary magnetic field by effects on the magnetic field at
513 synchronous orbit. *Journal of Geophysical Research: Space Physics*, *92*(A10),
514 11215-11220. doi: 10.1029/JA092iA10p11215
- 515 Petrukovich, A. A. (2009). Dipole tilt effects in plasma sheet b_y : statistical model
516 and extreme values. *Annales Geophysicae*, *27*(3), 1343–1352. doi: 10.5194/
517 angeo-27-1343-2009
- 518 Tenfjord, P., Østgaard, N., Snekvik, K., Laundal, K. M., Reistad, J. P., Haaland, S.,
519 & Milan, S. E. (2015). How the IMF B_y induces a B_y component in the closed
520 magnetosphere and how it leads to asymmetric currents and convection pat-
521 terns in the two hemispheres. *Journal of Geophysical Research: Space Physics*,
522 *120*(11), 9368-9384. doi: 10.1002/2015JA021579
- 523 Tenfjord, P., Østgaard, N., Strangeway, R., Haaland, S., Snekvik, K., Laundal,
524 K. M., . . . Milan, S. E. (2017). Magnetospheric response and reconfiguration
525 times following IMF B_y reversals. *Journal of Geophysical Research: Space*
526 *Physics*, *122*(1), 417-431. doi: 10.1002/2016JA023018
- 527 Thébault, E., Finlay, C. C., Beggan, C. D., Alken, P., Aubert, J., Barrois, O., . . .
528 Zvereva, T. (2015). International geomagnetic reference field: the 12th genera-
529 tion. *Earth, Planets and Space*, *67*(79). doi: 10.1186/s40623-015-0228-9
- 530 Tsyganenko, N. A. (2002a). A model of the near magnetosphere with a dawn-dusk
531 asymmetry 1. mathematical structure. *Journal of Geophysical Research: Space*
532 *Physics*, *107*(A8), SMP 12-1-SMP 12-15. doi: 10.1029/2001JA000219
- 533 Tsyganenko, N. A. (2002b). A model of the near magnetosphere with a dawn-
534 dusk asymmetry 2. parameterization and fitting to observations. *Journal of*
535 *Geophysical Research: Space Physics*, *107*(A8), SMP 10-1-SMP 10-17. doi:

- 536 10.1029/2001JA000220
537 Tsyganenko, N. A., & Andreeva, V. A. (2020). Magnetospheric penetration of
538 IMF viewed through the lens of an empirical RBF modeling. *Journal of Geo-*
539 *physical Research: Space Physics*, *125*(1), e2019JA027439. (e2019JA027439
540 10.1029/2019JA027439) doi: 10.1029/2019JA027439
- 541 Wing, S., Newell, P. T., Sibeck, D. G., & Baker, K. B. (1995). A large statis-
542 tical study of the entry of interplanetary magnetic field *y*-component into
543 the magnetosphere. *Geophysical Research Letters*, *22*(16), 2083-2086. doi:
544 10.1029/95GL02261
- 545 Woodfield, E. E., Dunlop, M. W., Holme, R., Davies, J. A., & Hapgood, M. A.
546 (2007). A comparison of cluster magnetic data with the tsyganenko 2001
547 model. *Journal of Geophysical Research: Space Physics*, *112*(A6). doi:
548 10.1029/2006JA012217